

Journal of Biomedical Optics

BiomedicalOptics.SPIEDigitalLibrary.org

Dual-wavelength laser speckle imaging for monitoring brain metabolic and hemodynamic response to closed head traumatic brain injury in mice

Itamar Kofman
David Abookasis

Dual-wavelength laser speckle imaging for monitoring brain metabolic and hemodynamic response to closed head traumatic brain injury in mice

Itamar Kofman and David Abookasis*

Ariel University, Department of Electrical and Electronics Engineering, Ariel 40700, Israel

Abstract. The measurement of dynamic changes in brain hemodynamic and metabolism events following head trauma could be valuable for injury prognosis and for planning of optimal medical treatment. Specifically, variations in blood flow and oxygenation levels serve as important biomarkers of numerous pathophysiological processes. We employed the dual-wavelength laser speckle imaging (DW-LSI) technique for simultaneous monitoring of changes in brain hemodynamics and cerebral blood flow (CBF) at early stages of head trauma in a mouse model of intact head injury ($n = 10$). For induction of head injury, we used a weight-drop device involving a metal mass (~50 g) striking the mouse's head in a regulated manner from a height of ~90 cm. In comparison to baseline measurements, noticeable dynamic variations were revealed immediately and up to 1 h postinjury, which indicate the severity of brain damage and highlight the ability of the DW-LSI arrangement to track brain pathophysiology induced by injury. To validate the monitoring of CBF by DW-LSI, measurements with laser Doppler flowmetry (LDF) were also performed ($n = 5$), which confirmed reduction in CBF following injury. A secondary focus of the study was to investigate the effectiveness of hypertonic saline as a neuroprotective agent, inhibiting the development of complications after brain injury in a subgroup of injured mice ($n = 5$), further demonstrating the ability of DW-LSI to monitor the effects upon brain dynamics of drug treatment. Overall, our findings further support the use of DW-LSI as a noninvasive, cost-effective tool to assess changes in hemodynamics under a variety of pathological conditions, suggesting its potential contribution to the biomedical field. To the best of our knowledge, this work is the first to make use of the DW-LSI modality in a small animal model to (1) investigate brain function during the critical first hour of closed head injury trauma, (2) correlate between injury parameters of LDF measurements, and (3) monitor brain hemodynamic and metabolic response to neuroprotective drug treatment. © 2015 Society of Photo-Optical Instrumentation Engineers (SPIE) [DOI: 10.1117/1.JBO.20.10.106009]

Keywords: closed head injury; laser speckle imaging; hemodynamics; cerebral blood flow, neuroprotective drug.

Paper 150334RR received May 17, 2015; accepted for publication Sep. 11, 2015; published online Oct. 22, 2015.

1 Introduction

Traumatic brain injury (TBI), a global health problem, is a highly complex disorder involving a large number of biochemical and metabolic changes leading to a cascade of pathophysiological events such as inflammation, necrosis, and excitotoxicity, resulting in tissue damage and neuronal cell death.¹⁻⁵ Over the years, substantial progress in both hardware and software has been made in conventional neuroimaging modalities, such as computed tomography (CT), magnetic resonance imaging (MRI), and positron emission tomography, to monitor and evaluate these pathological changes, each with its specific advantages and limitations.⁶⁻⁸ These techniques have revolutionized medical research and greatly advanced our understanding of the pathophysiological response to head injury; however, their routine use remains complex and expensive. In contrast to these modalities, optical tissue imaging techniques circumvent several limitations of conventional neuroimaging and possess specific advantages: they are relatively inexpensive, easy to operate, portable, and are free from the adverse effects of ionizing radiation.⁹ The advantages of optical imaging

techniques have garnered significant attention to their suitability to biomedical applications. These optical imaging platforms work on the principle that hemodynamic parameters, such as blood volume, oxygenation, concentration of hemoglobin, lipids, and water, as well as structural changes, can be measured indirectly by tissue's absorption and scattering coefficients.¹⁰ Thus, dynamic changes in brain tissue during the development and treatment of head injury can be detected and analyzed via changes in these primary coefficients. With that, many researchers were inspired to develop a variety of optical diagnostic methods for functional brain monitoring.¹¹

Prominent among these methods is dual-wavelength laser speckle imaging (DW-LSI) modality, first introduced in the pioneering study of Dunn et al., who were the first to utilize the combination of LSI and spectroscopic imaging in a single optical imaging instrumentation to characterize cerebral hemodynamic, oxygen metabolic, and blood flow changes in real time during cortical spreading depression and whisker stimulation in rats.¹² DW-LSI is a relatively inexpensive, simple, wide-field, and noncontact optical biomedical imaging modality that integrates the principles of laser flowmetry and oximetry to

*Address all correspondence to: David Abookasis, E-mail: davida@ariel.ac.il

obtain macroscopic information such as hemoglobin concentration and blood flow. These data are obtained by a single standard CCD camera collecting the diffused speckled light reflected from a sample illuminated by laser sources of two different light wavelengths. Thus, using the modified Beer-Lambert law,¹³ one can extract a range of tissue hemodynamic parameters from the collected light reflection data. Since the initial development of DW-LSI, several modifications and applications have been reported using this principle adopted by the biomedical optics community.^{14,15} As suggested recently, simultaneous changes in blood flow and metabolic oxygenation under physiological and pathological conditions (TBI, stroke, epilepsy, etc.) can be monitored optically with high spatiotemporal resolution utilizing DW-LSI.^{16,17}

The present work implements DW-LSI for investigation of brain pathophysiological changes during the first critical hour following closed head injury (CHI) in intact mouse head model. CHI is a type of TBI in which the brain is injured as a result of a blow to the head or a sudden, violent motion that causes the brain to move inside the skull.^{18,19} It is different from open head injury in that no object penetrates the intact skull. In this work, CHI was induced by the regulated impact of a 48 g cylindrical metallic rod upon the intact mouse scalp.²⁰ The mouse CHI model is used to study the cascade of neurophysiological deficits caused by CHI, leading to cell death.²¹ Since the layers of the mouse skull are optically thin and highly transparent to light, we consider the diffuse reflected signals to originate from the brain itself. During experiments, the anesthetized mouse head was irradiated continuously by two laser wavelengths before, during, and after the onset of injury. Captured images were analyzed to examine the spatiotemporal characteristics of a selected, clinically relevant battery of volume-averaged hemodynamic and metabolic parameters. Results indicate dynamic changes in brain physiological properties relative to baseline measurements, observed up to 1 h post-injury. Additionally, DW-LSI was applied to test the effect of the neuroprotective drug therapy with hypertonic saline (HTS) on brain function after injury. Furthermore, the variations in cerebral blood flow detected using DW-LSI were found to be similar to measurements obtained using a commercially available laser Doppler flowmetry device. Overall, our findings indicate that DW-LSI is a suitable platform for study of both normal and pathophysiological brain conditions, such that it holds promise for neuroscience research applications. The present work is part of a series of studies aimed to assess brain hemodynamic and metabolic markers during CHI in anesthetized rodents, using different optical platforms.^{22,23}

The continuation of this paper is organized as follows. Section 2 provides the experimental protocol, instrumentation setup, and data processing, including a brief review of the methods by which hemodynamic and metabolic parameters were estimated. Experimental results and discussion are presented in Sec. 3. Finally, in Sec. 4, we present a brief summary of results reported in this paper and consider the potential use of DW-LSI technique as a clinical diagnostic tool.

2 Materials and Methods

2.1 Animals and Injury Protocol

Animal procedure was performed in accordance with the regulations of the Institutional Animal Care and Use Committee of Ariel University, in accordance with the guidelines of the

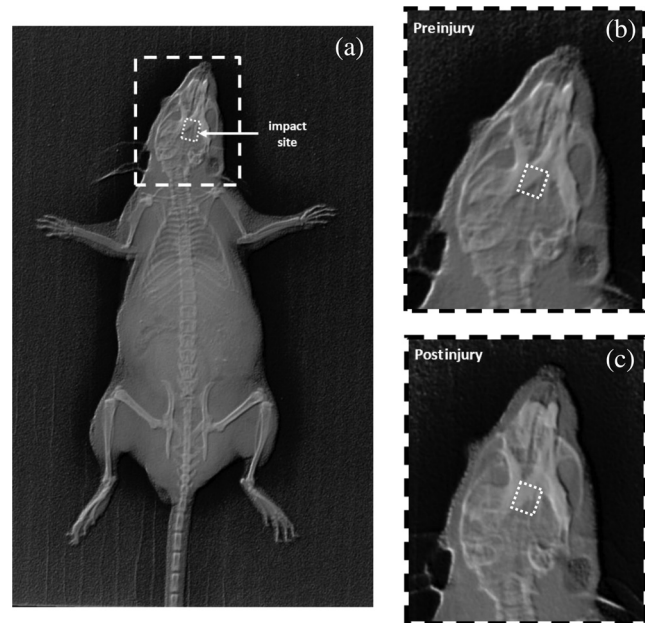


Fig. 1 Representative head photographs: (a) all body x-ray imaging. The small dotted line box indicates the impact site. Enlarged region of the head (b) before and (c) 30 min postinjury, as denoted by the large dotted box in (a). No structural damage or bruising to the head is seen following injury.

National Institute of Health. Twenty healthy male Sabra mice with an average body mass of 48 ± 4 g weight at 25 ± 1 weeks of age were used in the following experiments and housed in groups of four to five per cage in a 12 h:12 h light:dark cycle with a room at a controlled temperature of $22 \pm 1^\circ\text{C}$. Food and water were provided *ad libitum*. After anesthesia by intraperitoneal injection with a cocktail of ketamine (80 mg/kg), xylazine (20 mg/kg), and saline (NaCl, 0.9%), each mouse was restrained on an in-house-made stand, the head was immobilized, scalp hair carefully removed using a commercial hair removing lotion, and a sponge was inserted underneath the chin. Core body temperature was monitored continuously during the experiment using a thermocouple rectal probe and body temperature was maintained at $\sim 34^\circ\text{C}$ throughout experimentation. Respiratory activity and blood oxygen saturation (SpO_2) were monitored at regular intervals using a commercial pulse oximeter device (Nonin, 8600) attached to the forelimb. CHI was induced under anesthesia using a weight-drop apparatus including a vertical 1-m-long metal tube (inner diameter 13 mm) with a cylindrical metallic weight (48 g, length = 9.5 cm, $\Phi = 10$ mm) dropped through the tube from 87 cm directly above the intact mouse scalp, producing an impact of 4176 g cm between the anterior coronal suture (Bregma) and posterior coronal suture (Lambda). This model of injury closely mimics real-life focal head trauma and was shown to not produce structural brain damage.²¹ To validate that no physical damage occurred following weight impact, mouse heads were imaged using an x-ray system (Mobilett, Siemens) combined with a computerized radiography system (Kodak, CR360), before and after injury. Representative head photographs can be seen in Fig. 1; no contusion or hemorrhage is observed. Baseline reflectance measurements (15 min) were obtained prior to induction of injury, after which the mouse was placed under the weight-drop device orthogonally to the point of

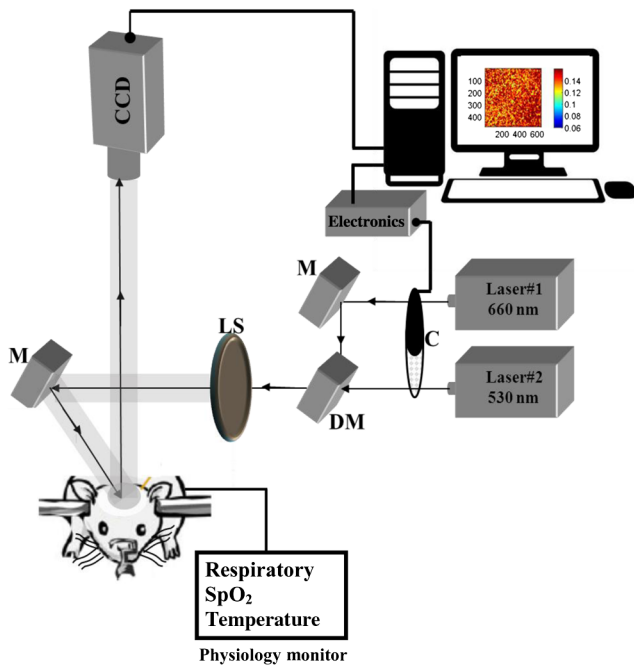


Fig. 2 Sketch of the dual-wavelength laser speckle imaging (DW-LSI) arrangement. Entire system was controlled using MATLAB® software on a personal computer. M, mirror; C, chopper; DM, dichroic mirror; LS, lens system; CCD, charge-coupled device camera.

impact. Immediately postinjury, the mouse was returned to the optical setup and the effects of injury were studied for 100 min and for another 30 min after single injection of anesthetic overdose, simple model of hypoxic ischemic brain injury (HIBI). Modification of this protocol following neuroprotective drug treatment (HTS) on new animal groups will be described later in detail in Sec. 3.

2.2 System Setup

A schematic representation of the experimental setup is presented in Fig. 2. Two laser beams from a diode laser operating at 530 and 660 nm, respectively, were switched on by an in-house-made filter chopper, such that only one laser wavelength was transmitted at one given time, allowing no illumination crosstalk. The filter chopper runs at a constant speed (1 Hz) and was synchronized with the CCD camera operated in the MATLAB® environment to acquire images at the appropriate wavelength. When the laser beam reaches the plate beam splitter, it is collimated and expanded by a lens system, and subsequently directed by a mirror to uniformly illuminate the scalp at an incident angle of ~ 40 deg from the head normal direction, such that specular reflections do not affect the measurements. By careful alignment of the optical elements in the illumination path, both wavelengths irradiate the same surface area of the head. The diffuse reflectance image from the head at each wavelength is recorded with a 14-bit CCD camera [Guppy PRO F-031B, 656(h) \times 494(v) pixel, 5.6 μ m pixel pitch, Allied Vision Technologies, Germany] connected to a PC and situated perpendicular to the head surface. The camera is equipped with a macro zoom lens (Computar, MLH10X, F5.6-32, Japan), positioned 16 cm above the head, which provides an adjustable magnification to guarantee (1) Nyquist criterion (speckle size \geq

$2 \times$ camera pixel size) necessary for flow imaging²⁴ and (2) a reasonable field of view ($\approx 10 \times 10$ mm²). Camera exposure time was set at 10 ms in order to optimize the contrast-to-noise ratio.^{25,26} Imaging acquisition, synchronization, and data processing are achieved using software implemented in the MATLAB® platform (Version 2010a, The MathWorks, Inc., Natick, Massachusetts) controlled via a personal computer (Intel Core, E6750). The captured images were stored automatically and sequentially into external memory for future image processing. It should be mentioned that several variables can limit the performance of this speckle imaging scheme, such as layer dynamics, systematic effects, depth of imaging, inherent frame-to-frame noise, speckle and pixel size, sampling window size, absorption and scattering coefficients of the medium, etc. A variety of solutions have been proposed to reduce many of these limitations.^{24,27–30} In addition, because of the limited penetration depth of this imaging modality, obtaining blood flow information and other physiological parameters from the human brain through the intact scalp, for example, is still challenging compared to conventional neuroimaging techniques.

2.3 Imaging Sampling

The intact mouse scalp was sequentially illuminated at 530 and 660 nm wavelengths and the remitted reflectance was captured by a single CCD camera (raw speckle images) and saved for offline processing and analysis with in-house scripts written in MATLAB® software. Two images at two different wavelengths were acquired in order to assess variation in tissue composition levels (diffuse reflectance spectroscopy concept). Throughout the experiments, the time interval between the images acquired from each wavelength was ~ 1 s. Imaging commenced before induction of CHI to establish baseline physiological parameters and continued during and following experimental intervention. Baseline images were obtained 15 min before injury induction, such that each mouse served as its own control. Imaging commenced ~ 3 min after CHI and continued for 100 min. Prior to data analysis, the collected diffuse images were first normalized to overcome the nonlinearity of the camera quantum efficiency at the above wavelengths, after which the images were digitally filtered (averaging filter using *fspecial* function in MATLAB®) to (1) remove periodic noise due to heart beat and respiration, (2) suppress speckle noise resulting from coherent illumination, and (3) to eliminate the high-frequency noise originating from the camera itself during recording. No other processing was applied to the images. It should be emphasized that the above filtering process was not applied for the flow analysis since it would reduce the information content in speckle patterns, and was used only as a preprocessing step before hemoglobin concentration calculation. A selected region of interest (ROI) with the impact site at its center was selected by the investigators for data processing.

2.4 Calculation of Hemodynamic and Metabolic Parameters

As noted before, DW-LSI integrates two wavelengths in an LSI setup to simultaneously image both the relative changes in blood flow (with 660 nm) and changes in hemodynamic parameters (with both 530 and 660 nm) over both space and time.¹⁵ After data collection and preprocessing as described in Sec. 2.3, a standard sliding-window algorithm (7×7 pixel

dimension) was applied to convert each 660 nm raw speckle image to a speckle contrast (K_s) image calculated by the ratio of the image's standard deviation (σ_s) to its mean intensity ($\langle I \rangle$).^{14,15}

$$K_s = \frac{\sigma_s}{\langle I \rangle} \propto \frac{1}{\sqrt{\bar{V}}}, \quad (1)$$

where \bar{V} is the mean cerebral blood flow (CBF) speed, such that lower speed results in higher K_s and vice versa. This K_s - \bar{V} relationship is true when the camera exposure time is higher than speckle decorrelation time.²⁶ Thus, blood flow dynamics were extracted from the reflectance images. For the reader's knowledge, transcranial Doppler ultrasonography is the most common noninvasive tool used clinically to estimate CBF.³¹ Other clinical flow measurement modalities, such as xenon CT and arterial spin labeling MRI, are also in use.³²

Simultaneously to flow measurements, temporal changes in concentrations of oxyhemoglobin (HbO₂) and deoxyhemoglobin (Hbr) were extracted from the diffuse reflectance data based on the Beer-Lambert law described below.^{12,33}

$$\begin{bmatrix} \Delta \text{HbO}_2(t) \\ \Delta \text{Hbr}(t) \end{bmatrix} = \begin{bmatrix} \epsilon_{\text{HbO}_2}^{530} & \epsilon_{\text{Hbr}}^{530} \\ \epsilon_{\text{HbO}_2}^{660} & \epsilon_{\text{Hbr}}^{660} \end{bmatrix}^{-1} \left\{ \begin{array}{l} \frac{\ln[R_{530}(0)/R_{530}(t)]}{D_{530}} \\ \frac{\ln[R_{660}(0)/R_{660}(t)]}{D_{660}} \end{array} \right\}, \quad (2)$$

where ϵ is the molar spectral absorbance coefficient of an absorbing chromophore, $R_{530}(t)$ and $R_{660}(t)$ are the measured diffuse reflectance values at time t for the two wavelengths after injury, and $R_{530}(0)$ and $R_{660}(0)$ are the baseline values prior to injury. D_{530} and D_{660} are the differential path length factors of the light inside the tissue.¹⁵ We assume that at the two wavelengths used in the present setup, (1) scattering is nearly constant and (2) other chromophores such as lipids, cytochrome-*c* oxidase, collagen, etc. contribute insignificantly to the absorption spectrum, relative to hemoglobin. The total hemoglobin concentration change can also be quantified by $\Delta \text{THC} = \Delta[\text{HbO}_2] + \Delta[\text{Hbr}]$. For the reader's knowledge, ΔTHC can give information about changes in cerebral blood volume (ΔCBV) and it is assumed to be linearly proportional to CBV , thus $\Delta \text{THC} \sim \Delta \text{CBV}$. We chose to record at 530 and 660 nm based on their sensitivity to THC and Hbr, respectively. At 530 nm (isosbestic point), HbO₂ and Hbr absorb light equally and the change in reflection is proportional to THC; THC can be readily obtained at this wavelength. At 660 nm, the absorption of HbO₂ is threefold less compared with the absorption of Hbr such that both can be easily calculated.

In addition to hemoglobin concentration changes and based on Eqs. (1) and (2), the relative changes in oxygen metabolism, known as cerebral metabolic rate of oxygen (CMRO₂), can be calculated.³⁴

$$r\text{CMRO}_2 \equiv \frac{\Delta \text{CMRO}_2(t)}{\text{CMRO}_2(o)} \propto \frac{(1 + r\text{CBF}) \times \left[1 + \gamma_R \frac{\Delta \text{Hbr}(t)}{\text{Hbr}(o)} \right]}{\left[1 + \gamma_T \frac{\Delta \text{THC}(t)}{\text{THC}(o)} \right]} - 1. \quad (3)$$

γ_R and γ_T are vascular weighting constants that are assumed to be 1 for simplification,¹² which is within a physiologically plausible range of 0.75 to 1.25.³⁵ $r\text{CBF}$ is the fractional change of CBF compared with baseline and is approximated by

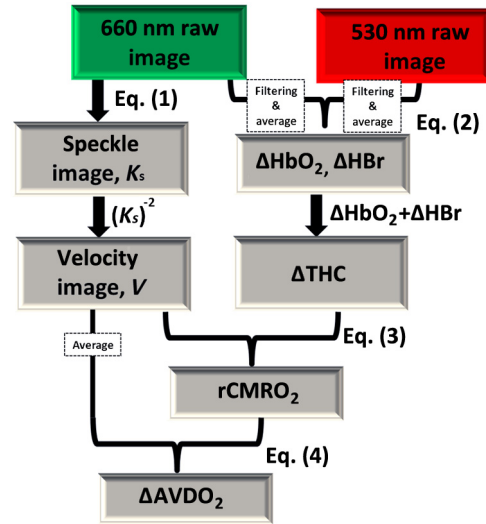


Fig. 3 Flow chart describing the estimation of different brain tissue properties. First, raw consecutive images at two wavelengths of illumination are acquired. Next, the flow image is obtained with the 660 nm image via Eq. (1). Concurrently, hemoglobin features are calculated through Eq. (2) using both images of 530 and 660 nm. Next, the combination of measured hemoglobin and blood flow was utilized to derive relative cerebral metabolic rate of oxygen (CMRO₂) by Eq. (3). Finally, based upon the cerebral blood flow (CBF) and CMRO₂ values, cerebral arteriovenous difference of oxygen (AVDO₂) is obtained by Eq. (4).

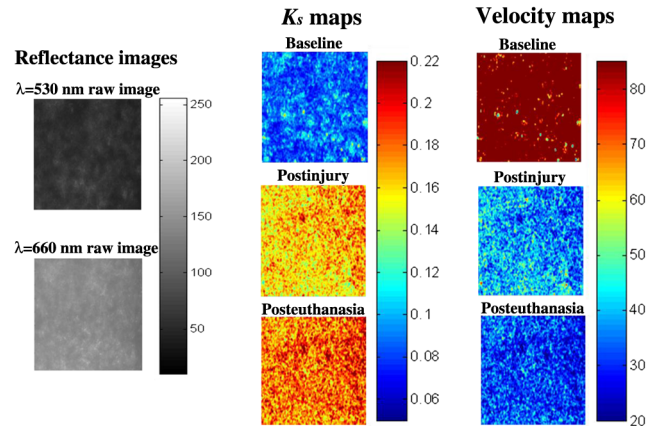


Fig. 4 Representative experimental raw speckle images at 530 and 660 nm (left) recorded from an intact mouse scalp, respectively, and the corresponding speckle contrast (K_s) (middle) and velocity (right) maps at representative time points. These maps were computed directly from raw speckle image (660 nm) using Eq. (1) with 7×7 areas of pixels.

$\Delta V(t)/V(o)$ calculated with Eq. (1). It has been shown that γ_R and γ_T do not influence the calculated $r\text{CMRO}_2$.³⁶ CMRO₂ (i.e., oxygen consumption) measures the difference between the rate of oxygen flowing into and out of a region of investigation.³⁷ CMRO₂ is a valuable tool in the clinical setting, as it helps to study brain function.³⁸ It is considered a function of mitochondrial activity and can be calculated from CBF and the arteriovenous oxygen content difference. To highlight relative changes over time, each individual image was averaged using *mean2* function in MATLAB®, providing a single mean value of individual pixel intensities within the entire ROI. Once the CBF and CMRO₂ values are available, cerebral

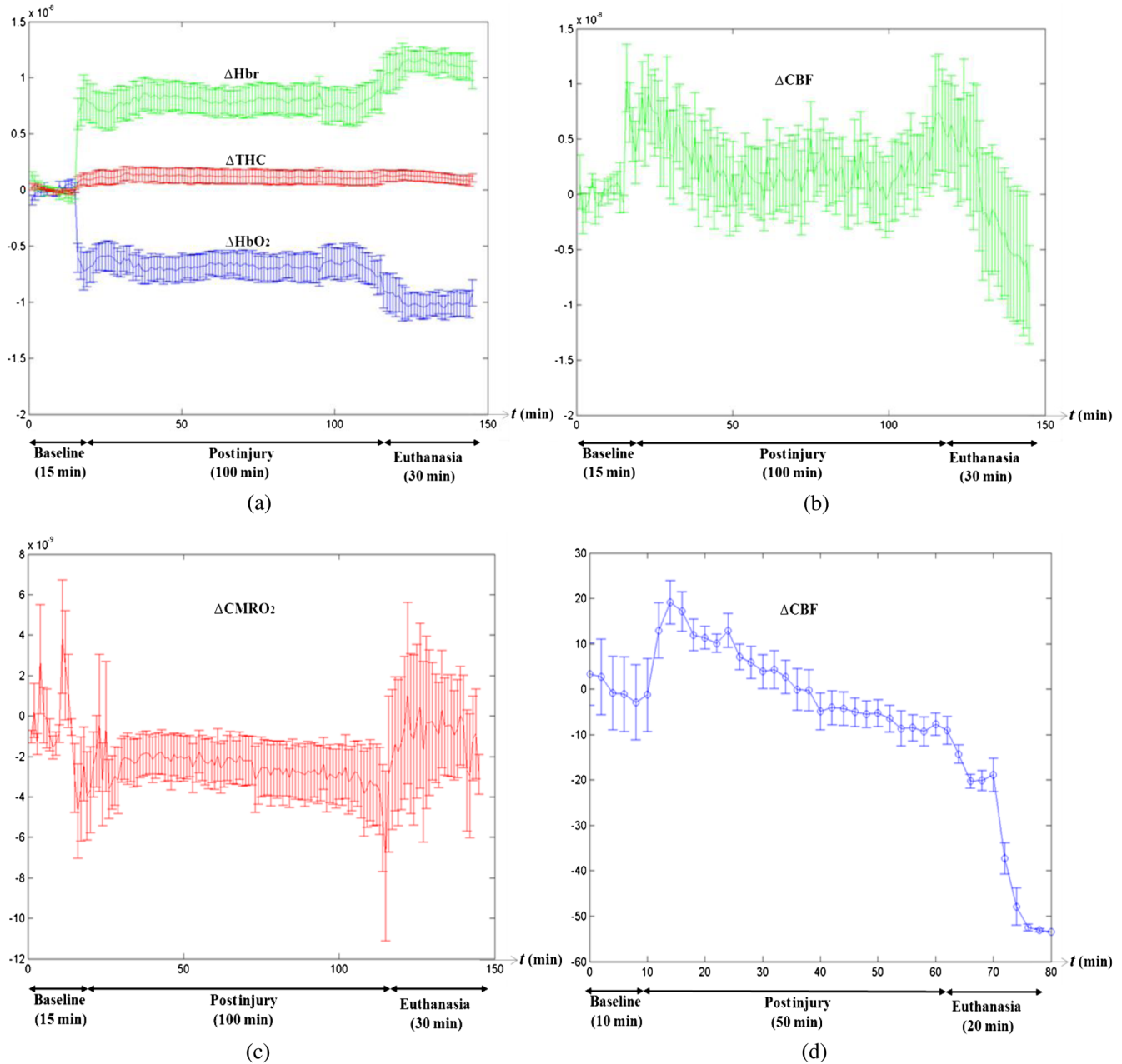


Fig. 5 Summary of hemodynamic and metabolic responses to closed head injury (CHI) as measured by the DW-LSI system: (a) time series of the changes in HbO_2 , Hbr , and THC ; (b) change in CBF over the entire time course; (c) CMRO_2 monitored using DW-LSI system as a function of time ($n = 10$); and (d) CBF measured by the laser Doppler flowmetry (LDF) probe ($n = 5$).

arteriovenous difference of oxygen (AVDO_2) can be obtained. AVDO_2 represents the amount of oxygen extracted by the brain, and reflects the balance between CMRO_2 and CBF calculated by^{39,40}

$$\Delta\text{AVDO}_2 = \frac{\Delta\text{CMRO}_2}{\Delta\text{CBF}}. \quad (4)$$

Overall, in the present study, a total of six hemodynamic and metabolic parameters can be derived simultaneously within specific areas of interest by the DW-LSI system: V (or K_s^{-2}), ΔHbO_2 , ΔHbr , ΔTHC (or ΔCBV), $r\text{CMRO}_2$, and ΔAVDO_2 . It should be pointed out that because of the partial volume

effect, we were able to obtain only relative changes in the above parameters over time, relative to baseline values, rather than their absolute values. The above steps are summarized in the block diagram illustrated in Fig. 3. In Fig. 4, representative raw images at two wavelengths used and speckle contrast and velocity maps at specific time point of baseline, postinjury, and euthanasia are presented, highlighting flow changes occur over time.

2.5 Statistical Analysis

All the data are expressed as mean \pm standard error, and two-way analysis of variation was performed to determine

significant differences in means. Results were judged to be statistically significant if the p value was <0.05 . Calculations were executed using MATLAB®'S Statistic Toolbox (Version 2010a, The MathWorks, Inc.).

3 Results and Discussion

Figures 5(a)–5(d) summarize the statistical analysis of changes in chromophore concentrations and metabolism properties over time in 10 animals at normal state (baseline), following brain injury challenge, and after overdose administration. Please note that the error bars (standard error) in all panels may represent the variation in the calculated mean reflectance for each ROI. These variations expressed as error bars can be explained by variability among individual tissue sample properties, as well as unavoidable variances due to breathing, involuntary muscle contraction, etc. Relative to baseline, a salient difference in a range of brain physiological properties was demonstrated. Viewing the outcomes revealed that progress from baseline to brain injury induces an abrupt increase in Hbr and decrease in HbO₂ [Fig. 5(a)], concurrently with slightly increased Δ THC (consequently, Δ CBV). The increase in Δ THC following injury appeared to be primarily due to the relative rise in deoxyhemoglobin concentration. It can be seen that the chromophore concentrations before and after injury are distinct across the experiment duration. These results appear to reflect the pathophysiology of the brain following trauma, which can lead to permanent brain damage, neurological disorders, or even death. The higher level of Hbr due to ongoing metabolic activity promotes the development of secondary brain damage stemming from ischemia, a common occurrence postinjury.^{3–5} The difference between Δ HbO₂ and Δ Hbr, expressed as Δ HbD,⁴¹ representing the mismatch between the two parameters, can serve as a marker of oxygen delivery. Indeed, Δ HbD was observed to decrease following injury. The slower rate of change in THC may have corresponded to decreased blood flow resistance in the injured area, as confirmed by Figs. 5(b) and 5(c).

Figure 5(b) represents the variation in CBF, derived as in Eq. (1) above. Three phases of spatial changes in CBF, which highlight the cerebral autoregulation (CAR) function, were observed: following the first few minutes after injury, blood flow increased and subsequently decreased toward its baseline level. In the homeostatic CAR process, arterioles undergo ongoing dilation and constriction, yielding cyclical changes in cerebral vascular resistance, in turn changing arterial blood pressure and cerebral perfusion to maintain a constant blood flow.^{42,43} Disturbed CAR can reduce the ability of the injured brain to preserve adequate blood flow, as observed in patients with mild to severe brain injuries.^{44,45} Generally speaking, impaired CAR adversely impacts clinical outcome and is associated with cerebrovascular abnormalities and increased mortality. The increases in blood flow we observed may be compensatory mechanisms, which serve to overcome the effect of the injury or as a result of the euthanasia injection.

Under decreased CBF, brain cells undergo a series of pathophysiological changes further complicated by disrupted oxygen balance, leading to disrupted extracellular ion concentrations, increased lactate levels, decreased extracellular pH, abnormal accumulation of glutamate, etc.⁴⁶ Studies of CBF in severe head-injured patients show that, among other factors, altered CBF levels are related to poor clinical outcome.⁴² The variations in CBF currently observed with the DW-LSI system were

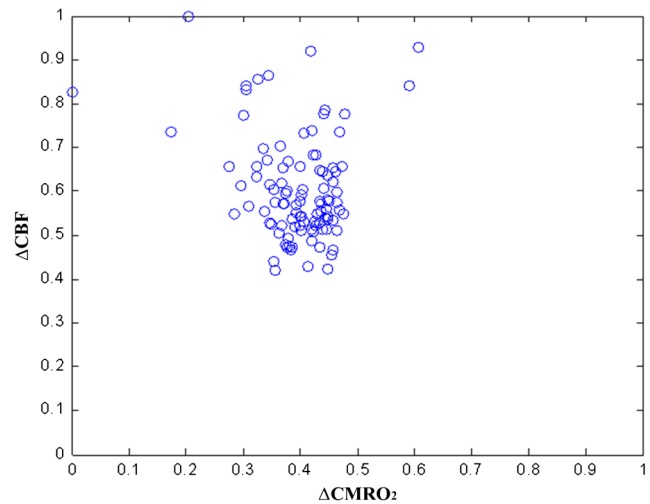


Fig. 6 Scatter plot showing correlation between r CMRO₂ and Δ CBF for entire experiments. To facilitate comparison, both Δ CBF and r CMRO₂ were normalized between 0 and 1 ($n = 10$).

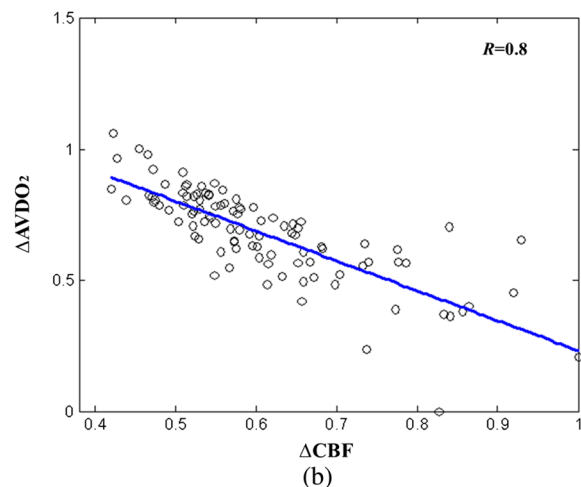
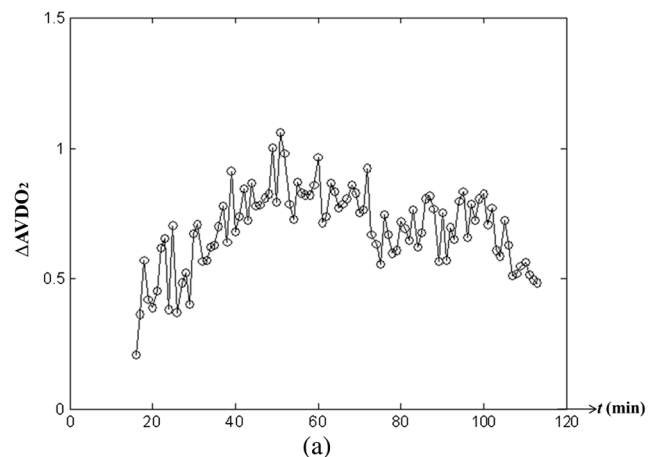


Fig. 7 Change in AVDO₂ during postinjury period: (a) dynamics of AVDO₂ postinjury and (b) Δ AVDO₂ versus Δ CBF following injury. The line is the best-fit linear regression (circles), with correlation $R^2 = 0.8$ ($n = 10$). The slope of the linear fit was -1.14 and the overall mean difference between the two was $\sim 8\%$.

confirmed using a laser Doppler flowmetry (LDF) probe (Periflux, PF 2B), as presented by Fig. 5(d). As demonstrated by both methodologies, CBF dropped after injury, indicating decreased oxygen delivery to the brain, which may result in permanent hypoxic brain damage. Similar changes in CBF following CHI in piglet brains were observed by Yodh's group during axonal injury [Ref. 47, Fig. 3(e)] and others reporting alterations in CBF following traumatic brain injury in both animal models and clinical findings.^{42,48}

In addition to the above panels, time-course assessment of the changes in oxygen metabolism (relative CMRO₂) is presented in Fig. 5(c). $r\text{CMRO}_2$, combining Figs. 5(a) and 5(b) according to Eq. (3), is considered an indicator of brain tissue viability. Figure 5(c) demonstrates an ~35% reduction in $r\text{CMRO}_2$ relative to baseline, suggesting metabolic suppression, mitochondrial dysfunction, and reduced oxygen consumption following injury. The average normal CMRO₂ is 1.5 $\mu\text{mol/g/min}$, and after head injury, it often falls to an average of 0.9 $\mu\text{mol/g/min}$,⁴⁹ a reduction of 40%, close to that observed presently. Several groups have reported a similar decrease in CMRO₂ in brain injury models during cerebral ischemia.^{36,50,51} Decreased CMRO₂ postinjury also indicates a reduction in electrocortical activity.^{52,53} Changes in metabolism and CBF tend to correlate tightly, such that increased metabolic demand is met rapidly by increased CBF and substrate delivery. These changes are thought to be controlled by several vasoactive metabolic mediators including hydrogen ions, potassium, CO₂,

adenosine, glycolytic intermediates, phospholipid metabolites, nitric oxide, etc. However, as observed here, the timecourse of CMRO₂ changes in head injury differs substantially from those observed in ΔCBF , such that $\Delta\text{CBF} > r\text{CMRO}_2$. This condition, known as cerebral hyperemia, is frequently seen in severe head injury patients and contributes to brain swelling and high intracranial pressure (ICP).⁵⁴ Although CBF and CMRO₂ share a common variable, they have been noted often not to be correlated in patients with head injuries. The uncoupling between these two parameters induced by head injury is believed to contribute to cerebral ischemia and cerebral hyperemia.⁴² Muizelaar et al. observed this uncoupling also among children suffering from head injury,⁵⁵ while Robertson et al. show that when coupled with elevated CBF, a higher CMRO₂ is associated with a better outcome (Ref. 56, Fig. 9). To facilitate comparison, both ΔCBF and relative $r\text{CMRO}_2$ were first normalized between 0 and 1 and presented relative to each other in Fig. 6. Since CMRO₂ possesses temporal dynamics different from those of hemodynamic response, both parameters together provide a more complete view on the

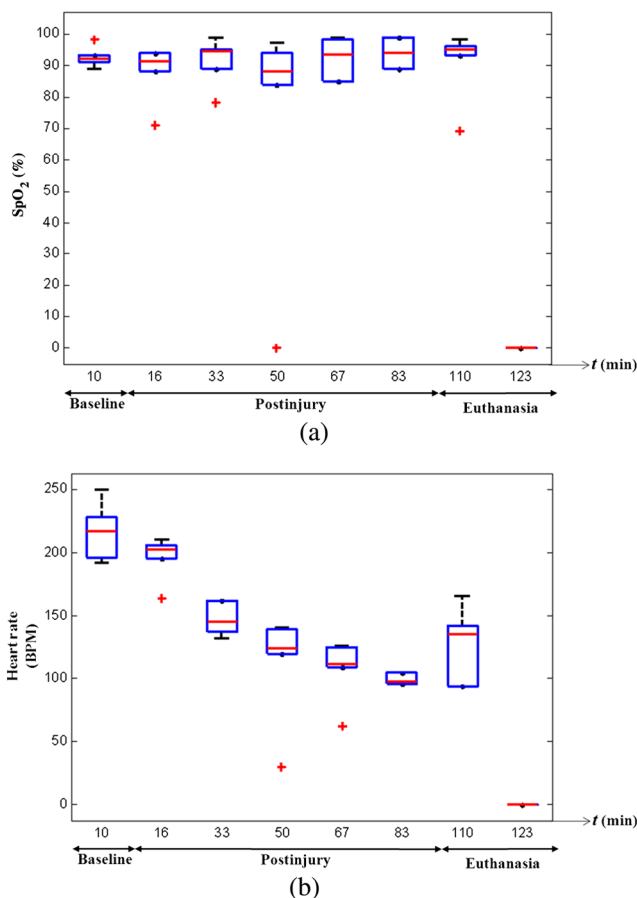


Fig. 8 Box plot graph displays the average values of (a) arterial oxygen saturation (SpO₂) and (b) heart rate (HR) at representative time points ($n = 10$).

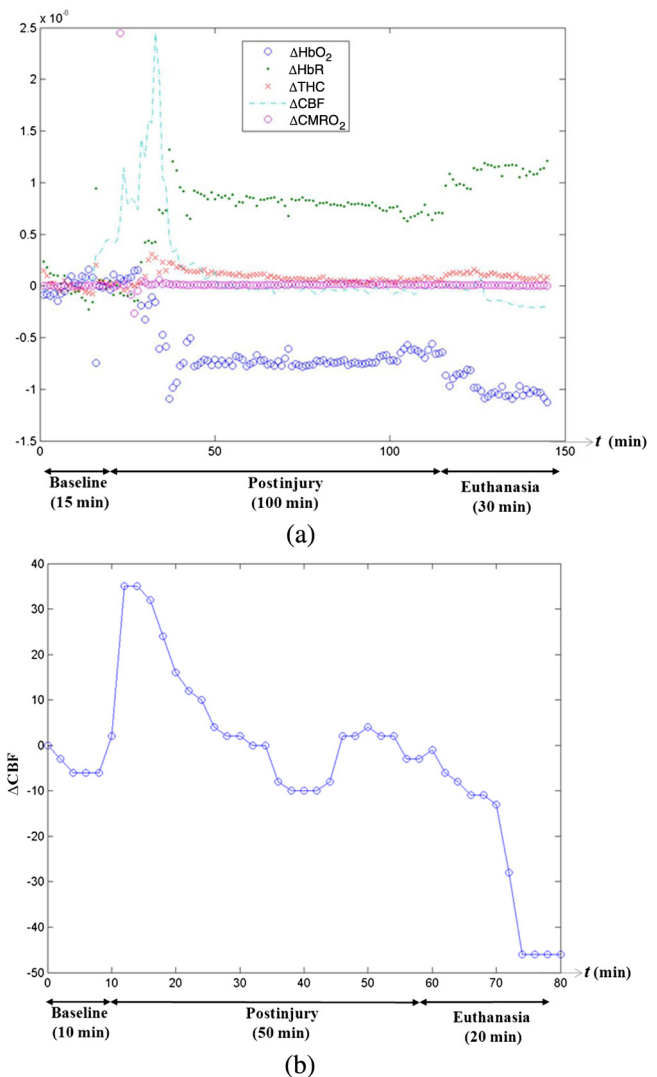


Fig. 9 Example plot of a representative mouse experiment. (a) Traces of hemodynamic and metabolic response following CHI and (b) change in CBF over the entire time course as measured by the LDF probe. Note similarity to DW-LSI results (Fig. 5(b)).

brain function following injury. The discrepancy between the two, presented in a scatter plot, documents the uncoupling between blood flow and cellular metabolism, which stems from variations in the cerebral oxygen extraction fraction.⁵⁷ The change in AVDO₂ during the postinjury period was analyzed and shown in Fig. 7. Δ AVDO₂ time course and its negative correlation to Δ CBF are presented in Figs. 7(a) and 7(b), respectively. Variations in Δ AVDO₂ following injury are believed to result from the changes observed in CBF. The correlation between AVDO₂ and CBF has been reported elsewhere.^{58,59}

As expected and shown in all figures, euthanasia (HIBI model) worsens both hemodynamic and metabolic parameters over time, causing a further decrease in the already limited blood supply to the injured zone, leading to permanent neuronal damage and finally death. HIBI most often results from insults such as cardiac arrest, vascular catastrophe, poisoning (i.e., drug overdose), or head trauma.⁶⁰ In our experiments, decreased oxygen delivery to the brain accompanied decreased cerebral perfusion, resulting in failure of autoregulation mechanisms and a severe decrease in cerebral blood flow over time.

The early changes reported during the injury and euthanasia periods delineate: (1) the pathophysiologic processes of the brain in response to CHI and overdose injection and (2) changes in brain hemodynamics and metabolism, in agreement with the results available in the literature,^{61–64} and (3) demonstrate the capability of DW-LSI to monitor dynamics of hemodynamics and metabolism during brain injury over time through the intact scalp. In addition to hemodynamics and metabolic activities, Fig. 8 presents box plots at representative time points of the heart rate (HR) and arterial oxygen saturation (SpO₂) values during the experiments. The HR was found to significantly decrease with time postinjury, which reflects the severity of

the injury model used, indicating that the damage reached the brainstem. SpO₂ fluctuated near its baseline level following injury and dropped following euthanasia, without any significant changes relative to baseline.

Brain parameters over time obtained from a representative mouse are illustrated in Fig. 9(a), alongside changes in CBF measured by the LDF setup [Fig. 9(b)]. The effects of injury and euthanasia are clearly visible and reflect the experiments outlined in Fig. 5. Figure 10 displays the speckled contrast map and its corresponded pixel histogram profile for baseline [Fig. 10(a)], following brain injury [Fig. 10(b)], and after overdose injection [Fig. 10(c)]. Each contrast map covers an area of $\sim 10 \times 10$ mm², corresponding to 656×492 pixels, resulting in an average spatial resolution of ~ 0.015 mm/pixel. The color bar to the right of each map indicates the K_s [Eq. (1)] value. As expected, spatiotemporal modification of the speckle patterns is apparent: as time elapses from the baseline, increased map contrast indicates decreased blood flow ($K_s \sim 1/\sqrt{V}$). In addition, we can observe from the histogram profile that each state is characterized with a characteristic peak value and distribution width (at half of peak height). Both parameters together may serve as an indicator of the brain's pathophysiological state.

Finally, the effects of the neuroprotective agent frequently used in intensive care and operating units for treatment of head injury, HTS,⁶⁵ was tested on injured mice ($n = 5$). HTS was arbitrarily selected among drugs in clinical use for treatment of head trauma.^{66–68} HTS is an osmotic agent administered intravenously to patients in the acute phase of severe TBI.^{69–71} It acts to reduce brain swelling and ICP by increasing the sodium levels in the bloodstream, thereby inducing a shift of fluid across the osmotic gradient it generates from the intracellular to the extracellular space. Shortly after administration, HTS reduces blood viscosity, which improves CBF and cerebral oxygenation,

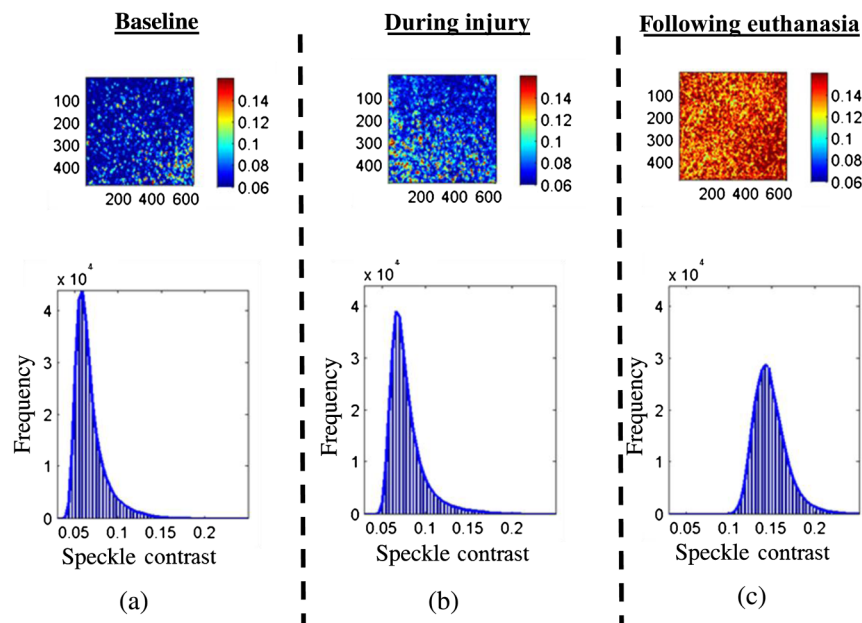


Fig. 10 Two-dimensional speckle contrast map and pixel histograms: (a) baseline, (b) injury period, and (c) following euthanasia. The scale bar on the right side of each map panel represents the speckle contrast value, K_s , of each pixel in the map. Map size is $\sim 10 \times 10$ mm, 656×492 pixels. As time elapses, the map contrast increase indicates decreased blood flow. Histograms showing the distribution of the K_s parameter value for the three states indicate the degree of spatial variation in K_s . The solid curve is a Gaussian fit with appropriate mean and standard deviation. In each state, peak value and distribution width of the histogram are modified, respectively.

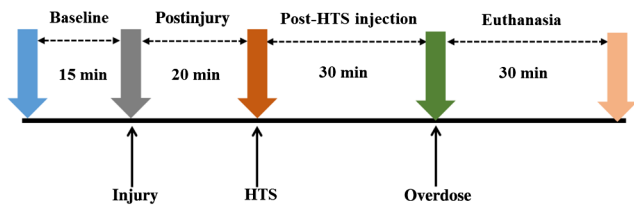


Fig. 11 Modified experimental protocol including hypertonic saline (HTS) injection.

causing autoregulatory vasoconstriction, thereby further reducing ICP.^{72,73} The protocol described in Sec. 2.1 was slightly modified for the HTS study: baseline measurements were obtained prior to induction of injury for 15 min, after which the mouse was removed and placed under the weight-drop device, and underwent focal TBI. Immediately postinjury, the mouse was returned to the optical setup and the effects of injury were studied 20 min post-trauma. At the end of the 20 min, a single injection of 5 $\mu\text{L/g}$ of 23.4% NaCl HTS was administered intraperitoneally and measurements were acquired for another 30 min. After 30 min, the mouse was sacrificed. This modified protocol is outlined in Fig. 11. Figure 12 presents the time course of hemodynamic and metabolic parameters of mice treated with HTS; an $\sim 20\%$ decrease in ΔHbr and an $\sim 25\%$ increase in ΔHbO_2 follow HTS injection. At the same time, both ΔCBF and $r\text{CMRO}_2$ increased gradually (Fig. 13) in contrast to mice not treated with HTS [Figs. 5(b) and 5(c)], suggesting a possible mechanism for the clinical neuroprotective properties of HTS. Increased CBF may be attributed to the decreased ICP and increased systemic blood pressure caused by HTS.⁷³ The correlation between ΔAVDO_2 and ΔCBF over time is presented in Fig. 14, and the differences pre- and post-HTS injection are demonstrated. As shown in the graph, HTS increases the linearity of the slope between the two states from 0.5 to 0.97, coupled with a correlation of $R = 0.78$ ($p < 0.05$). Increase in slope may highlight decrease in cell swelling and brain edema evolution. In addition, HR and SpO_2 measurements in Fig. 15 reveal that HTS treatment stabilizes both parameters in comparison to untreated mice (Fig. 8). In light of these results, we conclude that HTS successfully mitigated brain tissue damage in early stages postinjury. Nevertheless, further studies with

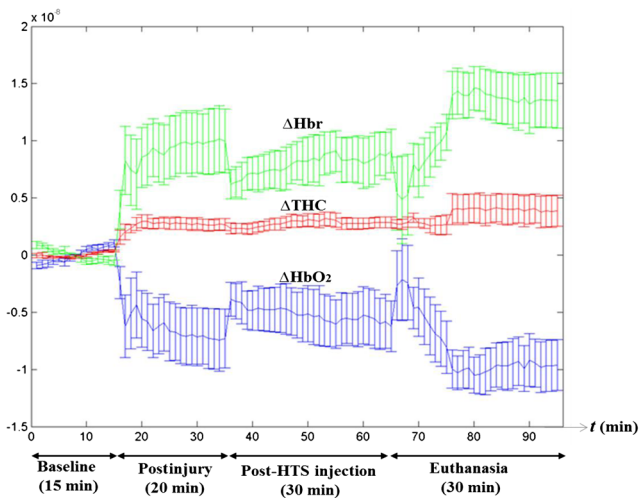


Fig. 12 Time series of hemodynamic and metabolic response following HTS injection. ΔHbr decreased by $\sim 20\%$ while ΔHbO_2 increased by $\sim 25\%$ following HTS injection ($n = 5$).

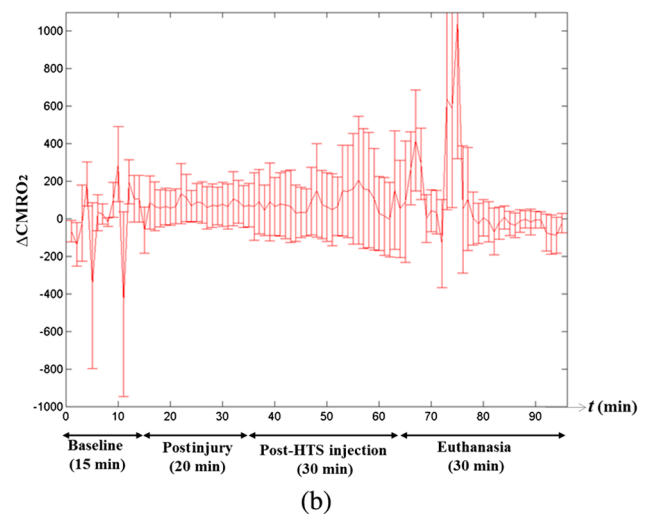
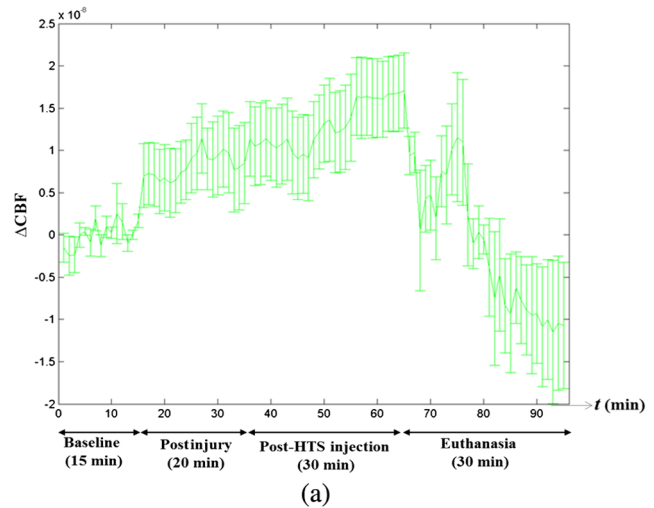


Fig. 13 Time series of the changes in (a) CBF and (b) CMRO_2 following the HTS protocol. Both metrics increased following HTS administration ($n = 5$).

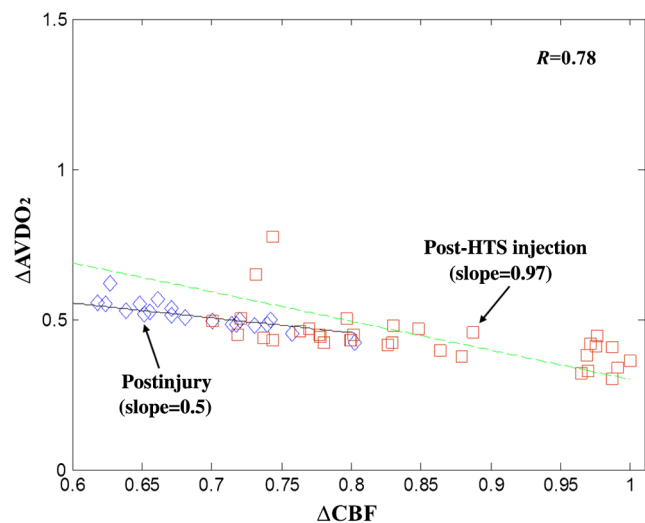


Fig. 14 Changes in AVDO_2 as a function of CBF postinjury and post-HTS injection. Data points represent measurements and lines represent linear fits to this data. HTS increases the linearity of the slope between the two from 0.5 to 0.97. Both parameters are in correlation: $R = 0.78$.

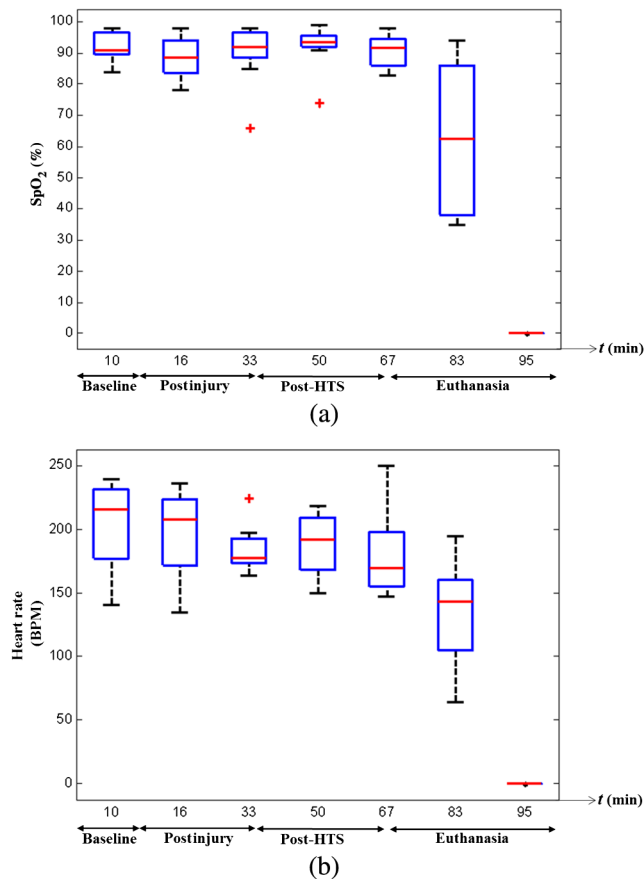


Fig. 15 Box plot graphs show the average values of (a) SpO_2 and (b) HR at representative time points following the HTS protocol. HTS treatment stabilizes both parameters in comparison to Fig. 8 ($n = 5$).

larger animal populations are needed in order to further elucidate the effects of HTS treatment, which will be elaborated in our ongoing research.

4 Conclusion

In the present study, we demonstrated the feasibility of a DW-LSI approach to simultaneously and continuously measure brain hemodynamic and metabolic parameters in a mouse model of intact TBI. In addition to application of DW-LSI to head injury treatment, the ability to continuously monitor the dynamics of hemodynamic and metabolic parameters may also aid the optimization treatment of cerebral hemorrhage or aneurism. To this end, we also demonstrated that DW-LSI can be utilized to study brain pathophysiology in a mouse model of HIBI. In addition, the effectiveness of HTS as a neuroprotective drug to reduce brain tissue damage was evaluated with DW-LSI. The ability to continuously monitor such neuro-pathophysiological parameters immediately after injury and following therapeutic strategies serves a critical clinical need, enabling the management of proper treatment. Therefore, DW-LSI may be further developed as a low-cost, noninvasive, and noncontact imaging modality for monitoring neuropathology in clinical settings. In the near future, larger-scale experiments are warranted to further elucidate our findings. Additionally, our ongoing research is aimed to test the capability of DW-LSI to monitor other pathological parameters of the brain, in concert with other optical and/or conventional approaches.

References

1. M. R. Bullock and J. T. Povlishock, "Guidelines for the management of severe traumatic brain injury," *J. Neurotrauma* **24**, S1–S106 (2007).
2. M. Faul et al., *Traumatic Brain Injury in the United States: Emergency Department Visits, Hospitalizations and Deaths 2002–2006*, Centers for Disease Control and Prevention National Center for Injury Prevention and Control, Atlanta, Georgia (2010).
3. J. H. Adams, D. I. Graham, and T. A. Gennarelli, "Head injury in man and experimental animals: neuropathology," *Acta Neurochir. Suppl. (Wien)* **32**, 15–30 (1983).
4. T. K. McIntosh et al., "Neuropathological sequelae of traumatic brain injury: relationship to neurochemical and biomechanical mechanisms," *Lab. Invest.* **74**(2), 315–342 (1996).
5. C. O. de Oliveira, N. Ikuta, and A. Regner, "Outcome biomarkers following severe traumatic brain injury," *Rev. Bras. Ter. Intensiva* **20**(4), 411–421 (2008).
6. B. F. Feyen et al., "Neuromonitoring in traumatic brain injury," *Minerva Anesthesiol.* **78**(8), 949–958 (2012).
7. S. H. Friess, T. J. Kilbaugh, and J. W. Huh, "Advanced neuromonitoring and imaging in pediatric traumatic brain injury," *Crit. Care Res. Pract.* **2012**, 1–11 (2012).
8. T. H. Le and A. D. Gean, "Neuroimaging of traumatic brain injury," *Mt. Sinai J. Med.* **76**, 145–162 (2009).
9. J. G. Fujimoto and D. L. Farkas, *Biomedical Optical Imaging*, Oxford University Press, Oxford, New York (2009).
10. D. A. Boas, C. Pitris, and N. Ramanujam, *Handbook of Biomedical Optics*, CRC Press, Boca Raton, Florida (2011).
11. E. M. C. Hillman, "Optical brain imaging in vivo: techniques and applications from animal to man," *J. Biomed. Opt.* **12**(5), 051402 (2007).
12. A. K. Dunn et al., "Simultaneous imaging of total cerebral hemoglobin concentration, oxygenation, and blood flow during functional activation," *Opt. Lett.* **28**(1), 28–30 (2003).
13. R. V. Maikala, "Modified Beer's law—historical perspectives and relevance in near-infrared monitoring of optical properties of human tissue," *Int. J. Ind. Ergon.* **40**(2), 125–134 (2010).
14. Z. Luo et al., "Simultaneous imaging of cortical hemodynamics and blood oxygenation change during cerebral ischemia using dual-wavelength laser speckle contrast imaging," *Opt. Lett.* **34**(9), 1480–1482 (2009).
15. J. Wang et al., "Dual-wavelength laser speckle imaging to simultaneously access blood flow, blood volume, and oxygenation using a color CCD camera," *Opt. Lett.* **38**(18), 3690–3692 (2013).
16. J. Qin et al., "Fast synchronized dual-wavelength laser speckle imaging system for monitoring hemodynamic changes in a stroke mouse model," *Opt. Lett.* **37**(19), 4005–4007 (2012).
17. Z. Yuan et al., "Imaging separation of neuronal from vascular effects of cocaine on rat cortical brain in vivo," *NeuroImage* **54**(2) 1130–1139 (2011).
18. J. T. E. Richardson, *Clinical and Neuropsychological Aspects of Closed Head Injury*, 2nd ed., Psychology Press, Philadelphia, Pennsylvania (2002).
19. R. L. Rodnitzky and M. Meier, "Neurobehavioral consequences of closed head injury," *Arch. Neurol.* **39**(10), 675–676 (1982).
20. M. A. Flierl et al., "Mouse closed head injury model induced by a weight-drop device," *Nat. Protoc.* **4**(9), 1328–1337 (2009).
21. O. Zohar et al., "Closed-head minimal traumatic brain injury produces long-term cognitive deficits in mice," *J. Neurosci.* **118**(4), 949–955 (2003).
22. D. Abookasis, A. Shochat, and M. S. Mathews, "Monitoring hemodynamic and morphologic responses to closed head injury in a mouse model using orthogonal diffuse near-infrared light reflectance spectroscopy," *J. Biomed. Opt.* **18**(4), 045003 (2013).
23. D. Abookasis, B. Volkov, and M. S. Mathews, "Closed head injury-induced changes in brain pathophysiology assessed with near-infrared structured illumination in a mouse model," *J. Biomed. Opt.* **18**(11), 116007 (2013).
24. D. A. Boas and A. K. Dunn, "Laser speckle contrast imaging in biomedical optics," *J. Biomed. Opt.* **15**(1), 011109 (2010).
25. S. Yuan et al., "Determination of optimal exposure time for imaging of blood flow changes with laser speckle contrast imaging," *Appl. Opt.* **44**(10), 1823–1830 (2005).
26. A. Fercher and J. Briers, "Flow visualization by means of single exposure speckle photography," *Opt. Commun.* **37**(5), 326–329 (1981).

27. D. Briers et al., "Laser speckle contrast imaging: theoretical and practical limitations," *J. Biomed. Opt.* **18**(6), 066018 (2013).
28. T. B. Rice et al., "Quantitative, depth-resolved determination of particle motion using multi-exposure, spatial frequency domain laser speckle imaging," *Biomed. Opt. Express* **4**(12), 2880–2892 (2013).
29. J. Qiu et al., "Correcting speckle contrast at small speckle size to enhance signal to noise ratio for laser speckle contrast imaging," *Opt. Express* **21**(23), 28902–28913 (2013).
30. D. Ringuette et al., "Reducing misfocus-related motion artefacts in laser speckle contrast imaging," *Biomed. Opt. Express* **6**(1), 266–276 (2015).
31. H. van Santbrink et al., "Serial transcranial Doppler measurements in traumatic brain injury with special focus on the early posttraumatic period," *Acta Neurochir.* **144**(11), 1141–1149 (2002).
32. K. Zhang et al., "Comparison of cerebral blood flow acquired by simultaneous [15O] water positron emission tomography and arterial spin labeling magnetic resonance imaging" *J. Cereb. Blood Flow Metab.* **34**(8), 1373–1380 (2014).
33. C. W. Du et al., "Simultaneous detection of blood volume, oxygenation, and intracellular calcium changes during cerebral ischemia and reperfusion in vivo using diffuse reflectance and fluorescence," *J. Cereb. Blood Flow Metab.* **25**(8), 1078–1092 (2005).
34. M. Jones et al., "Concurrent optical imaging spectroscopy and laser-Doppler flowmetry: the relationship between blood flow, oxygenation, and volume in rodent barrel cortex," *Neuroimage* **13**(6 Pt 1), 1002–1015 (2001).
35. D. A. Boas et al., "Can the cerebral metabolic rate of oxygen be estimated with near-infrared spectroscopy?," *Phys. Med. Biol.* **48**(15), 2405–2418 (2003).
36. P. B. Jones et al., "Simultaneous multispectral reflectance imaging and laser speckle flowmetry of cerebral blood flow and oxygen metabolism in focal cerebral ischemia," *J. Biomed. Opt.* **13**(4), 044007 (2008).
37. G. E. Cold, "Cerebral metabolic rate of oxygen (CMRO₂) in the acute phase of brain injury," *Acta Anaesthesiol. Scand.* **22**(3), 249–256 (1978).
38. A. K. Dunn et al., "Spatial extent of oxygen metabolism and hemodynamic changes during functional activation of the rat somatosensory cortex," *Neuroimage* **27**(2), 279–290 (2005).
39. P. D. Le Roux et al., "Cerebral arteriovenous oxygen difference: a predictor of cerebral infarction and outcome in patients with severe head injury," *J. Neurosurg.* **87**(1), 1–8 (1997).
40. W. D. Obrist et al., "Cerebral blood flow and metabolism in comatose patients with acute head injury. Relationship to intracranial hypertension," *J. Neurosurg.* **61**(2), 241–253 (1984).
41. G. Bale et al., "A new broadband near-infrared spectroscopy system for in-vivo measurements of cerebral cytochrome-c-oxidase changes in neonatal brain injury," *Biomed. Opt. Express* **5**(10), 3450–3466 (2014).
42. Y. Udomphorn, W. M. Armstead, and M. S. Vavilala, "Cerebral blood flow and autoregulation after pediatric traumatic brain injury," *Pediatr. Neurol.* **38**(4), 225–234 (2008).
43. M. Czosnyka et al., "Cerebral autoregulation following head injury," *J. Neurosurg.* **95**(5), 756–763 (2001).
44. G. E. Sviri et al., "Time course for autoregulation recovery following severe traumatic brain injury," *J. Neurosurg.* **111**(4), 695–700 (2009).
45. G. E. Sviri and D. W. Newell, "Cerebral autoregulation following traumatic brain injury," *Open Neurosurg. J.* **3**, 6–9 (2010).
46. A. Zauner and J. P. Muizelaar, "Brain metabolism and cerebral blood flow;" Chapter 5 in *Head Injury: Pathophysiology and Management of Severe Closed Injury*, P. Reilly and R. Bullock, Eds., pp. 89–99, Chapman and Hall, London (1997).
47. C. Zhou et al., "Diffuse optical monitoring of hemodynamic changes in piglet brain with closed head injury," *J. Biomed. Opt.* **14**(3), 034015 (2009).
48. I. Yamakami and T. K. McIntosh, "Alterations in regional cerebral blood flow following brain injury in the rat," *J. Cereb. Blood Flow Metab.* **11**(4), 655–660 (1991).
49. J. P. Muizelaar and M. L. Schröder, "Overview of monitoring of cerebral blood flow and metabolism after severe head injury," *Can. J. Neurol. Sci.* **21**(2), S6–S11 (1994).
50. Y. Tsuda et al., "Effect of hypocapnia on cerebral oxygen metabolism and blood flow in ischemic cerebrovascular disorders," *Eur. Neurol.* **27**(3), 155–163 (1987).
51. J. D. Winter et al., "Changes in cerebral oxygen consumption and high-energy phosphates during early recovery in hypoxic-ischemic piglets: a combined near-infrared and magnetic resonance spectroscopy study," *Pediatr. Res.* **65**(2), 181–187 (2009).
52. S. J. Lee et al., "Fetal cerebral blood flow, electrocorticographic activity, and oxygenation: responses to acute hypoxia," *J. Physiol.* **587**(Pt 9), 2033–2047 (2009).
53. K. M. Tichauer et al., "Cerebral metabolic rate of oxygen and amplitude-integrated electroencephalography during early reperfusion after hypoxia-ischemia in piglets," *J. Appl. Physiol.* **106**(5), 1506–1512 (2009).
54. Z. Muttaqin et al., "Hyperaemia prior to acute cerebral swelling in severe head injuries: the role of transcranial Doppler monitoring," *Acta Neurochir.* **123**(1–2), 76–81 (1993).
55. J. P. Muizelaar et al., "Cerebral blood flow and metabolism in severely head-injured children: part 1: relationship with GCS score, outcome, ICP, and PVI," *J. Neurosurg.* **71**(1), 63–71 (1989).
56. C. S. Robertson et al., "Cerebral blood flow, arteriovenous oxygen difference, and outcome in head injured patients," *J. Neurol. Neurosurg. Psychiatry* **55**(7), 594–603 (1992).
57. M. N. Diringer et al., "Regional cerebrovascular and metabolic effects of hyperventilation after severe traumatic brain injury," *J. Neurosurg.* **96**(1), 103–108 (2002).
58. F. Xu, Y. Ge, and H. Lu "Noninvasive quantification of whole-brain cerebral metabolic rate of oxygen (CMRO₂) by MRI," *Magn. Reson. Med.* **62**(1), 141–148 (2009).
59. V. Jain, M. C. Langham, and F. W. Wehrli, "MRI estimation of global brain oxygen consumption rate," *J. Cereb. Blood Flow Metab.* **30**(9), 1598–1607 (2010).
60. K. M. Busl and D. M. Greer, "Hypoxic-ischemic brain injury: pathophysiology, neuropathology and mechanisms," *NeuroRehabilitation* **26**(1), 5–13 (2010).
61. M. Prins et al., "The pathophysiology of traumatic brain injury at a glance," *Dis. Model Mech.* **6**, 1307–1315 (2013).
62. C. Werner and K. Engelhard, "Pathophysiology of traumatic brain injury," *Br. J. Anaesth.* **99**(1), 4–9 (2007).
63. G. J. Bouma and J. P. Muizelaar, "Cerebral blood flow in severe clinical head injury," *New Horiz.* **3**(3), 384–394 (1995).
64. T. P. Bouzat et al., "Beyond intracranial pressure: optimization of cerebral blood flow, oxygen, and substrate delivery after traumatic brain injury," *Ann. Intensive Care* **3**(1), 23–31 (2013).
65. D. S. Mortimer and J. Jancik, "Administering hypertonic saline to patients with severe traumatic brain injury," *J. Neurosci. Nurs.* **38**(3), 142–154 (2006).
66. D. J. Loane and A. I. Faden, "Neuroprotection for traumatic brain injury: translational challenges and emerging therapeutic strategies," *Trends Pharmacol. Sci.* **31**(12), 596–604 (2010).
67. I. Maas, "Neuroprotective agents in traumatic brain injury," *Expert Opin. Investig. Drugs* **10**(4), 753–767 (2001).
68. A. Singh, P. Sharma, and S. Mishra, "Neuro-protection after traumatic brain injury: novel strategies," *J. Dent. Med. Sci.* **3**(6), 75–85 (2013).
69. A. Bhardwaj and J. A. Ulatowski, "Hypertonic saline solutions in brain injury," *Curr. Opin. Crit. Care* **10**(2), 126–131 (2004).
70. S. Berger and R. Hartl, "Traumatic brain injury and use of hypertonic solutions," *Transfus. Altern. Transfus. Med.* **6**(4), 59–68 (2005).
71. D. S. Mortimer and J. Jancik, "Administering hypertonic saline to patients with severe traumatic brain injury," *J. Neurosci. Nurs.* **38**(3), 142–154 (2006).
72. H. White, D. Cook, and B. Venkatesh, "The use of hypertonic saline for treating intracranial hypertension after traumatic brain injury," *Anesth. Analg.* **102**(6), 1836–1846 (2006).
73. M. M. Mortazavi et al., "Hypertonic saline for treating raised intracranial pressure: literature review with meta-analysis," *J. Neurosurg.* **116**(1), 210–221 (2012).

Biographies for the authors are not available.